Förster, M., Haaland, S. (2015): Interhemispheric differences in ionospheric convection: Cluster EDI observations revisited. - *Journal of Geophysical Research*, *120*, 7, p. 5805-5823.

DOI: http://doi.org/10.1002/2014JA020774

AGU PUBLICATIONS

JGR

Journal of Geophysical Research: Space Physics

RESEARCH ARTICLE
10.1002/2014JA020774

Interhemispheric differences in ionospheric convection: Cluster EDI observations revisited

M. Förster[1] and S. Haaland[2,3]

[1]German Research Centre for Geosciences, Helmholtz Centre Potsdam, Potsdam, Germany, [2]Max-Planck Institute for Solar Systems Research, Göttingen, Germany, [3]Birkeland Centre for Space Science, University of Bergen, Bergen, Norway

Key Points:
- Average cross polar potential drop is slightly larger at the SH compared to NH
- North-south asymmetries of electric field pattern are mainly due to IMF By
- The thermospheric dynamo feedback results in further hemispheric differences

Correspondence to:
M. Förster,
mfo@gfz-potsdam.de

Citation:
Förster, M., and S. Haaland (2015), Interhemispheric differences in ionospheric convection: Cluster EDI observations revisited, *J. Geophys. Res. Space Physics*, *120*, 5805–5823, doi:10.1002/2014JA020774.

Received 27 OCT 2014
Accepted 30 APR 2015
Accepted article online 6 MAY 2015
Published online 14 JUL 2015

Abstract The interaction between the interplanetary magnetic field and the geomagnetic field sets up a large-scale circulation in the magnetosphere. This circulation is also reflected in the magnetically connected ionosphere. In this paper, we present a study of ionospheric convection based on Cluster Electron Drift Instrument (EDI) satellite measurements covering both hemispheres and obtained over a full solar cycle. The results from this study show that average flow patterns and polar cap potentials for a given orientation of the interplanetary magnetic field can be very different in the two hemispheres. In particular during southward directed interplanetary magnetic field conditions, and thus enhanced energy input from the solar wind, the measurements show that the southern polar cap has a higher cross polar cap potential. There are persistent north-south asymmetries, which cannot easily be explained by the influence of external drivers. These persistent asymmetries are primarily a result of the significant differences in the strength and configuration of the geomagnetic field between the Northern and Southern Hemispheres. Since the ionosphere is magnetically connected to the magnetosphere, this difference will also be reflected in the magnetosphere in the form of different feedback from the two hemispheres. Consequently, local ionospheric conditions and the geomagnetic field configuration are important for north-south asymmetries in large regions of geospace.

1. Introduction

Interaction between the solar wind and the dayside terrestrial magnetopause causes a transfer of energy and momentum from the solar wind to the magnetosphere. The interaction is particularly effective when the interplanetary magnetic field (IMF) has a southward orientation. The resulting reconnection with the geomagnetic field causes a large-scale circulation of plasma in the magnetosphere [*Dungey*, 1961]. This process can be described in terms of opening of magnetic flux on the dayside magnetopause and corresponding closure of flux in the nightside plasma sheet.

Since the magnetosphere is magnetically connected to the ionosphere, a corresponding circulation of plasma is also set up in the high-latitude ionosphere. This magnetic connection provides as well a feedback from the ionosphere to the magnetosphere. Consequently, the ionosphere exerts some control in the form of resistance to the magnetospheric circulation.

Prior to and within the early years of the space era, most of our knowledge about properties and processes in the ionosphere was obtained from ground-based measurements from the Northern Hemisphere (NH). The sparse number of observatories in the Southern Hemisphere (SH) polar cap region and their geographic distribution made it at that time difficult to investigate details or assess persistent north-south asymmetries using ground-based instrumentation alone. With the progress of systematic monitoring of the near-Earth space environment by long-term polar-orbiting missions and the deployment of a large number of observatories in the SH, in particular in the Antarctic, the observational situation has improved. Some studies focusing on conjugate effects exist, but many of them are case studies or from localized regions.

Pinnock et al. [1999] presented one of the first conjugate studies of ionospheric convection. Using ground-based radars, they were able to study the ionospheric flow simultaneously in both hemispheres for a 4 h period around local noon. They noted a significant asymmetry in the average flow direction, with the main flow channels rotated in opposite directions in north and south. The asymmetry was attributed to dayside reconnection in the presence of an IMF B_y component.

Yeoman et al. [2000] discuss convection responses to IMF B_y and B_z during substorm pseudobreakups. The results are based on HF (Super Dual Auroral Radar Network (SuperDARN)) and essentially look as time evolution. *Wild et al.* [2003] used SuperDARN from NH and SH to study the ionospheric response to a specific flux transfer event observed by Cluster. They did not focus specifically on NH differences but related the difference in NH and SH to the positive IMF B_y conditions prevailing.

Nishitani et al. [2003] combined HF data from Antarctica and ion drift measurements from the Defence Meterological Satellite Program (DMSP) to study the asymmetry under very quiet conditions during a 2 day period on 11–12 May 1999. They found strong asymmetries, with the dark ionosphere often characterized by localized high-speed flow events ($V > 1500$ m/s in the SH). They primarily attributed this to asymmetry in solar illumination in the two hemispheres.

Grocott et al. [2005], also using ground-based radar observations, presented two case studies of ionospheric response to tail reconnection. In both cases, a north-south asymmetry with oppositely directed convection bursts in the two hemispheres was observed. The observations were interpreted as a result of reconnection in an asymmetric tail under the prolonged influence of IMF B_y.

Watanabe et al. [2007] claims that the interhemispheric asymmetry stems from reconnection of overdraped lobe field lines and closed flankside field lines. This type of north-south asymmetric reconnection does not affect the merging cell potentials in the same hemisphere as the reconnection point, whereas in the opposite hemisphere, it diminishes the potential of the dawnside (or duskside) large-scale convection cell.

A study of intherhemispheric differences in dayside convection during northward IMF condition was conducted by *Wilder et al.* [2011]. They presented a case study in which reverse convection was simultaneously visible in the NH and SH near the northern winter solstice. For this event, they found that the convection along the noon meridian was significantly faster in the summer hemisphere (south). They had a strong negative IMF B_x, which would favor lobe reconnection and thus higher circulation in the NH. They claim that this is not enough though and that the axial tilt of the Earth was the dominant effect on convection.

The radial (i.e., B_x) component of the IMF also produces north-south asymmetries trough a combination of high-latitude (lobe) reconnection and enhanced solar wind dynamo action. *Förster et al.* [2013] found an indication for diverging potential differences between pairs of opposite IMF B_x orientation in the dayside high-latitude convection cells only, which are typical for northward IMF (IMF $B_z > 0$). They appear to be larger for an antiparallel orientation of the magnetic field of the magnetospheric tail and the solar wind (i.e., IMF $B_x < 0$ in the NH and vice versa in the SH). Statistical studies of auroral luminosity [e.g., *Liou et al.*, 1998; *Liou*, 2010; *Reistad et al.*, 2014] have shown that this asymmetry is also reflected in the polar cap ionosphere during negative IMF B_z conditions and it is associated with an increased solar wind dynamo efficiency in the respective hemisphere.

Properties of the ionosphere itself, such as conductivity, temperature, and density vary on several timescales, primarily due to variations in solar illumination and ionization. For a given time period or a given event, local ionospheric conditions can cause significant north-south asymmetries, even if there are little or no asymmetry in the external drivers [e.g., *Liou et al.*, 1998; *Østgaard et al.*, 2005].

The role of the neutral atmosphere for north-south asymmetries has also been recognized for decades. *Barlier et al.* [1974] used a large volume of data (temperatures, densities, concentrations, and winds) and noted that in addition to the annual variations, which can be explained by asymmetries in solar illumination, more energy seemed to be available for the thermosphere in the SH during equinoxes. They not only suggested that this asymmetry was due to an asymmetry in the geomagnetic field but also speculated whether dissipation of tidal waves induced by an asymmetrical worldwide ozone distribution could contribute to north-south asymmetries.

More recent results have also emphasized the role of the neutral atmosphere and the strong north-south asymmetry in the geomagnetic field. *A et al.* [2012] used satellite data and observed larger variations in the thermospheric density in the SH and suggested that a lower magnetic field there may allow stronger ion flows. Collisions will transfer energy and momentum between neutrals and ions, thereby causing more Joule heating and larger variations in the thermospheric density in south. A similar view was argued by *Förster and Cnossen* [2013]. Their results demonstrated that the north-south asymmetry in the geomagnetic field, both in strength and in orientation, could cause substantial hemispheric differences both in plasma drift and even more in the neutral wind magnitude and vorticity in the high-latitude upper thermosphere.

In this paper we focus on interhemispheric differences and long time (solar cycle) variations in the ionospheric convection. The results are based on measurements from the Electron Drift Instrument (EDI) on board the Cluster spacecraft. The study is partly based on our own earlier EDI-based studies presented in *Haaland et al.* [2007] and *Förster et al.* [2007]. Those papers only covered about 6 years of data and did not focus on north-south asymmetries or solar cycle influence. The improvement of this study consists of, first of all, about a factor of 2 better data coverage and thus more reliable evidences for the smaller hemispheric differences. Given the long-term data set that spans over one solar cycle, we address also the question of solar cycle dependence.

The paper is organized as follows: In section 2, we provide a brief description of the EDI data set and methodology. In section 3, we present results in terms of ionospheric convection patterns and polar cap potentials. Section 4 discusses implications of the results with a special emphasis on north-south differences, as well as solar cycle effects. Section 5 contains a short, pointwise summary of the main results from the study.

2. Data and Methodology

Our investigation is based on measurements from the European Space Agency (ESA) Cluster mission [*Escoubet et al.*, 1997]. Cluster is an ESA mission consisting of four identical spacecraft flying in a tetrahedron like formation and was launched into an approximately $4 \times 20 R_E$ polar orbit with an inclination of about 87°. The orbital period is around 57 h, and the spacecraft thus spend significant time in the magnetospheric lobe and polar cap regions, which are magnetically connected to the high-latitude polar cap regions. Full local time coverage is obtained within half a year. At the time of writing, Cluster has been in operation for more than 14 years, corresponding to more than one full solar cycle.

The methodology to derive the ionospheric convection from satellite measurements basically follows the same scheme used by *Haaland et al.* [2007] and *Förster et al.* [2007]. We will refer to these papers throughout the text, and to avoid unnecessary repetition, we will hereafter simply refer to these papers as H07 and F07, respectively. In those papers, convection data collected over a period of 6 years were used to derive characteristic average ionospheric plasma flow patterns and their cross polar cap potential (CPCP) as a function of solar wind parameters and geomagnetic activity indices.

For convenience, we briefly describe the data set and methodology of the H07 and F07 papers, but for a more comprehensive explanation, including detailed assessment of data quality, errors, and variability in the data, we refer to the original papers.

2.1. Convection Measurements From the Cluster EDI

As in the H07 and F07 papers, convection measurements used in the present paper are based on data from the Cluster EDI. We refer to the papers by *Paschmann et al.* [2001] and *Quinn et al.* [2001] for detailed instrument descriptions and capabilities of the instrument. In the present study, we use EDI data covering the years 2001–2013, i.e., more than a full solar cycle.

EDI provides very accurate measurements of the local electric field by measuring the drift of an electron beam within one gyroperiod. The EDI team commonly refers to this gyrocenter displacement as a *drift step*. In domains, where the magnetic field gradient is small, the drift is proportional to the convective electric field. This is the case for large fractions of the Cluster orbits, and in particular, the lobe and polar cap regions are of interest for us. Since both the magnetic field and the drift step can be determined with high precision, EDI provides very accurate measurements of the electric field. Unlike other techniques based on measurements in one direction or in one plane only (e.g., the line of sight-based radar measurements, or cross-track measurements from low-orbit satellites), EDI provides full vector measurements of the electric field. A further advantage of EDI is that the instrument is not affected by potential wake effects caused by spacecraft charging in tenuous plasma regimes [*Eriksson et al.*, 2006].

2.2. Mapping the Convection Electric Field

To study the ionospheric convection, we assume steady state conditions and equipotential magnetic field lines. We can then map an individual electric field measurement from Cluster altitudes in the magnetosphere to a plane at 400 km altitude in the polar cap ionosphere. For this purpose, we use the Tsyganenko T01 magnetic field model [*Tsyganenko*, 2002a, 2002b], properly parametrized with the prevailing solar wind and IMF conditions.

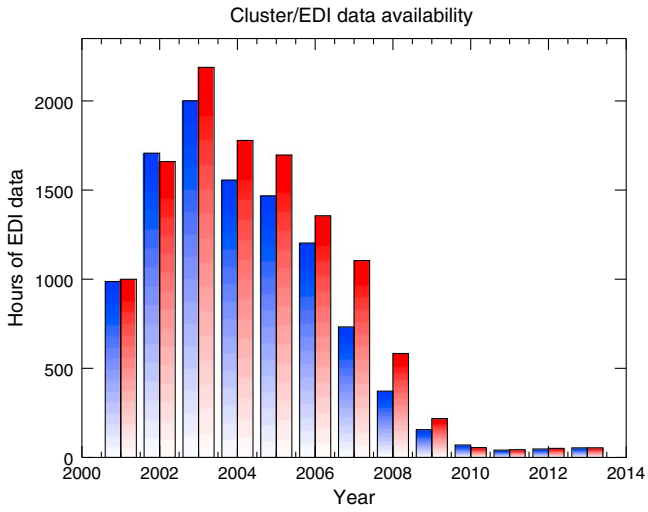

Figure 1. Yearly coverage of mapped Standard Processing (SP) EDI data. Blue (red) bars indicate number of data hours mapped to the Northern (Southern) Hemisphere.

The actual mapping procedure follows the same scheme as in the H07 and F07 papers. Basically, we use the measured electric and magnetic field to find the potential difference between two points at different field lines; one at Cluster and one point at an adjacent field line a certain distance away. From the magnetic field model we then establish the ionospheric foot points of these two points. The potential difference between the two field lines are then used to find the electric field in the ionosphere.

Typically, the mapping process involves not only a scaling of the electric field magnitude, given by the converging magnetic field, but also a change in orientation given by twists and bends in the magnetic field. We used Altitude Adjusted Corrected Geomagnetic (AACGM) coordinates [cf., e.g., *Gustafsson*, 1984; *Baker and Wing*, 1989] for the mapping and the binning in the ionosphere. Due to the nondipolar terms of the geomagnetic field, this coordinate system is nonorthogonal to a considerable amount at polar latitudes [e.g., *Laundal and Gjerloev*, 2014]. Our mapping procedure considers therefore an affine transformation of the observed electric field vector onto the magnetic northward and eastward components perpendicular to the local magnetic field at 400 km altitude. For details and illustration of the mapping procedure as well as the motivation and justification for using a magnetic field model, we refer to the H07 and F07 papers again.

Mapping was possible for the large majority of the EDI measurements, but for some cases, the magnetic field model could not be parametrized due to gaps in the solar wind data or the mapping itself failed. For a number of cases, the T01 model suggested closed field lines; in those cases, we were able to map the observed *E* field to *both* hemispheres. This ensures better coverage, in particular at lower latitudes, as compared to that in the original H07 and F07 papers.

Figure 1 shows the distribution of mapped Standard Processing (SP) EDI data of Cluster SC1–SC3 over the 13 years included in this study. The SP data had already been used in H07/F07 and are composed of 1 min averages of high-quality EDI measurements. In total, the updated data set consists of 10,400 h of electric field measurements mapped to the NH and 11,800 h mapped to the SH. This is about twice as much as for the original H07/F07 study (see Table 1 in H07). In this study, we will also make use of the EDI Prime Parameter (PP) data set that consists of spin-averaged observations (~4 s resolution). They total up to ~7.9 m and ~8.8 m data points for the NH and SH, respectively.

As a result of the apsidal precession of the orbit of Cluster since its launch, there is a better data coverage in the SH. The decline in the data coverage after 2003 can partly be explained by changes in the orbits and thus a shift of the satellite foot point away from the polar cap regions and partly by degradation and failure of some of the EDI sensors over time. There are not sufficient data in the declining data coverage years to establish reliable and complete potential patterns annually. Therefore, we combined several years of data acquisition for potential field considerations, in particular for the years of low solar activity. Alternatively, we considered average values of measured cross polar cap ion drift velocities within the polar cap that could be considered as a proxy for the CPCP values (cf. F07, Figures 7–9).

Table 1. Cross Polar Cap Potential (CPCP) Drop Between the Main Cells of the Statistical Plasma Drift Patterns Obtained From Mapped Spin-Resolution EDI Cluster Measurements (PP Data) for Eight Separate IMF Sectors[a]

		Cross Polar Cap Potentials, CPCP (kV)					
		2001–2013		2001–2003		2005–2010	
IMF		All Data		High Solar Activity		Low Solar Activity	
No. of Sector	Direction	NH	SH	NH	SH	NH	SH
0	B_z+	19.0	16.0	17.4	21.1	21.1	15.0
1	B_z+/B_y+	27.0	24.4	35.7	44.9	27.6	23.3
2	B_y+	43.8	42.4	54.3	51.3	42.5	38.6
3	B_z-/B_y+	57.7	57.1	70.7	72.2	53.9	53.1
4	B_z-	65.0	70.2	77.6	85.5	60.9	61.9
5	B_z-/B_y-	61.9	65.0	65.2	75.8	58.0	54.8
6	B_y-	42.6	42.1	47.8	49.7	37.6	39.5
7	B_z+/B_y-	22.7	26.7	27.2	31.3	24.4	24.1

[a]The first two data columns comprise the whole interval of EDI measurements obtained up to now (February 2001 to December 2013) for both the NH and SH; the middle pair of columns are from the initial period of high solar activity (2001–2003), and the final pair of columns shows the low solar activity conditions (2005–2010).

2.3. From Electric Field to Potential Pattern

At 400 km altitude, collisions and kinetic effects in the plasma are usually negligible, and a magnetohydrodynamic (MHD) description can be used to describe the plasma motion, i.e., $\vec{V} = \vec{E} \times \vec{B}/|B|^2$, where $\vec{V}, \vec{E}, \vec{B}$ are the plasma velocity, the electric field and the magnetic field, respectively.

Furthermore, by using the relation $E = -\nabla\Phi$, where Φ is the electrostatic potential, the convection can be described in terms of potentials. This approach has been applied to a number of studies, in particular radar-based studies using the Super Dual Auroral Radar Network (SuperDARN), and this has become a standard way of visualizing the large-scale convection at high latitudes [*Ruohoniemi and Baker*, 1998; *Ruohoniemi and Greenwald*, 2005; *Pettigrew et al.*, 2010; *Cousins and Shepherd*, 2010].

The interpretation of such potential plots is simple: convection is along the potential contours, and the distance between the contour lines indicates flow velocity. The original convection patterns were published in Figures 7 and 8 of the H07 paper for the NH and the SH, respectively. The presentation there is identical to that in this paper (Figures 2 and 3). Unfortunately, the potential values published in H07 and F07 were subject to a bug in the singular value decomposition (SVD) code that resulted in a systematic underestimation of the polar cap potential values of about 20% to 25%.

3. Results

In the following, we use the much extended EDI data set to revisit some of the analysis in H07 and F07, with special emphasize on north-south differences. Since we now have more than a full solar cycle of data, we also investigate whether any solar cycle effects are discernible in the convection patterns and CPCPs.

3.1. IMF Dependence of the Large-Scale Convection

Figures 2 and 3 show color-coded ionospheric convection patterns organized according to IMF orientation in the form of eight clock angle sectors of 45° width (for convenience, numbered from 0 to 7). Each panel shows the convection pattern for a given range of IMF direction and thus represents the overall average motion of plasma in the ionosphere for that given IMF orientation. Minimum and maximum potential values of the main cells as well as the resulting total CPCP are indicated in each panel.

The most prominent large-scale features, observed in both hemispheres, are the two-cell convection pattern for southward IMF and a four-cell pattern for purely northward IMF directions (sector 0). The latter is more pronounced in the NH. The symmetry axis of the four-cell convection pattern in the SH appears to be distorted due to a more extended duskside main cell. This hemispheric difference in the lobe cell convection at high latitudes seems to be significant. It might be related to a slightly larger clockwise offset toward negative clock

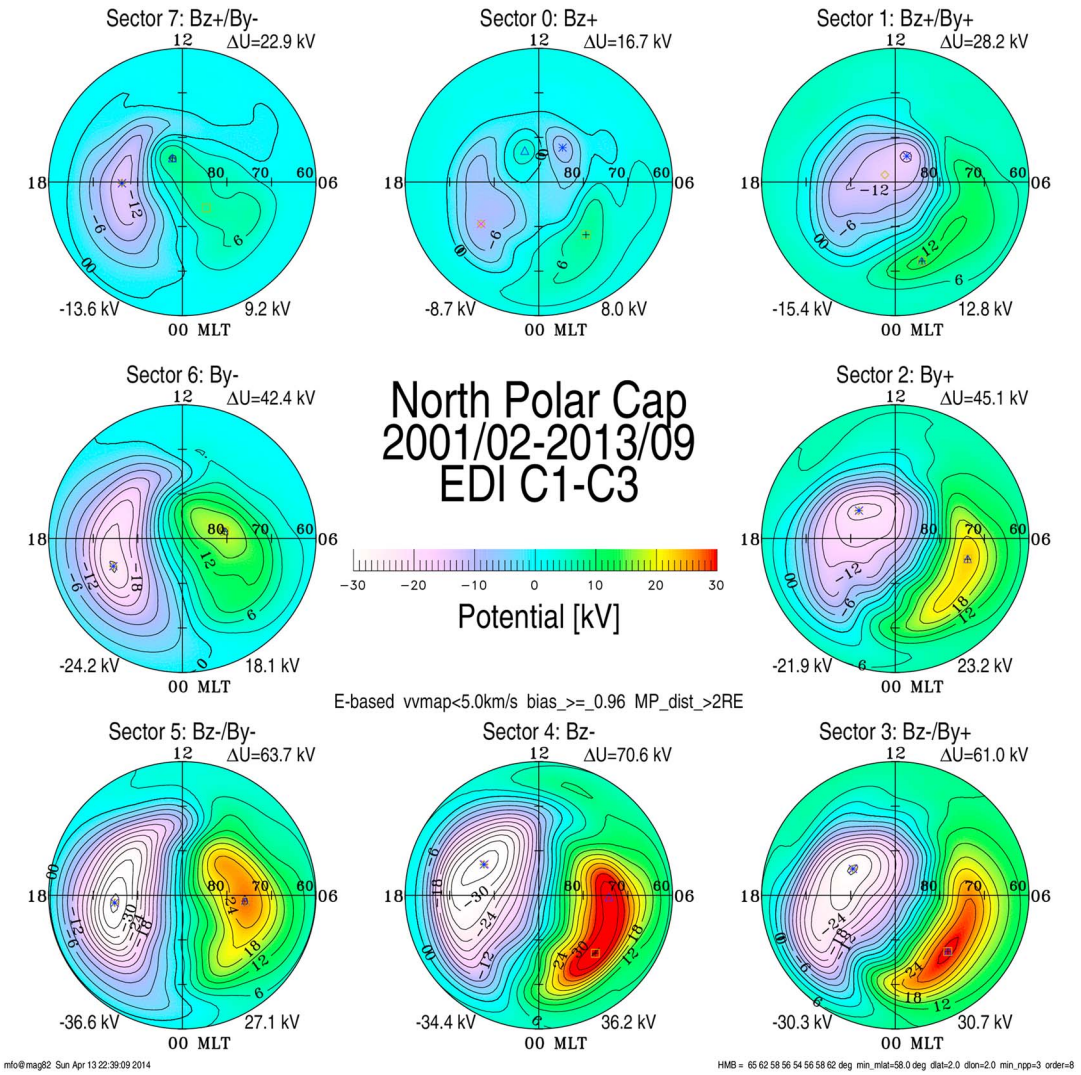

Figure 2. EDI (SP)-based ionospheric convection patterns in the NH for eight different orientations of IMF. Colors indicate potential values as indicated by the color bar in the middle. Contour lines are drawn for every 3 kV. The minimum and maximum potential for the main cells of each IMF direction is indicated at the bottom of each individual panel, and the total difference (cross polar cap potential, CPCP) is given in the top right of each individual panel.

angles in the SH that was found by *Förster et al.* [2008a]. Below, in section 3.4, we show further indications for subtle differences between the NH and SH for northward IMF conditions.

For positive IMF B_y (sectors 1–3), we see a clockwise rotation with a crescent-shaped dawn cell and a larger, more circular dusk cell in the NH. A slight clockwise rotation is still present for purely southward IMF conditions (sector 4). Correspondingly, for negative IMF B_y values (sectors 5–7), the rotation is anticlockwise, although not so pronounced as for positive IMF B_y values, and it even vanishes for sector 5 (see Figure 2). The dawn-dusk asymmetry was pointed out also in H07 and F07 and is mainly attributed to the IMF B_y stress and to gradients in the ionospheric conductivity [*Atkinson and Hutchison*, 1978; *Tanaka*, 2001; *Walsh et al.*, 2014].

To the first order, the corresponding IMF B_y response for the SH is a mirror image of the NH. A slight clockwise rotation can likewise be noticed for purely southward IMF (sector 4), while the rotation of the two-cell convection pattern vanishes in the SH for positive IMF B_y and negative B_z (sector 3) conditions (see Figure 3). In this sense, a dawn-dusk asymmetry caused by IMF B_y penetration will also lead to a north-south effect, as the convection pattern in the two hemispheres will be rotated in opposite directions. We will discuss implications of the IMF B_y penetration further in section 4.1.

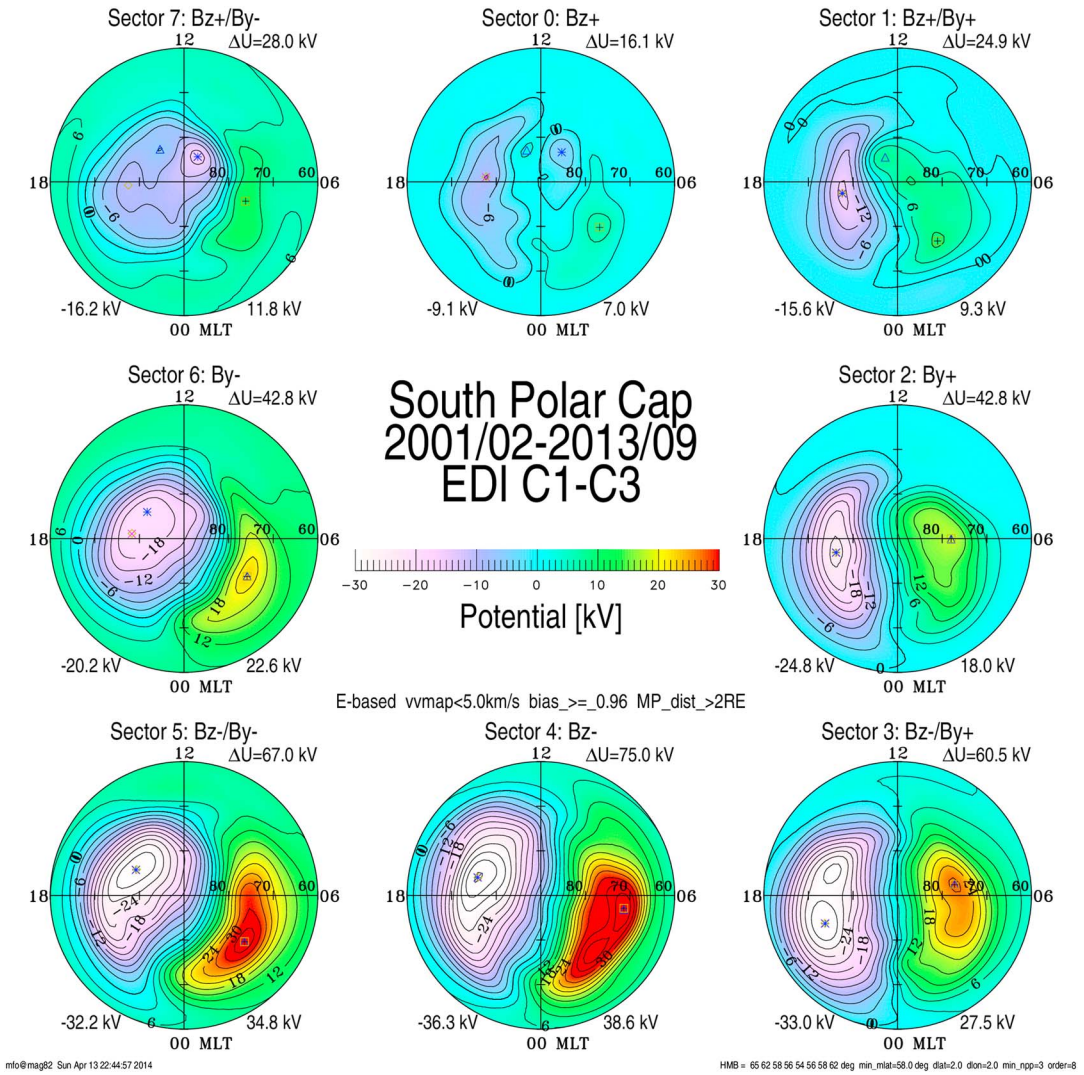

Figure 3. Same as Figure 2 but for the SH.

As clearly evident from Figures 2 and 3, the orientation of the IMF and its strength are the most important parameters for the solar wind-magnetosphere interaction, as they largely control the dayside-merging electric field [e.g., *Reiff et al.*, 1981; *Sonnerup et al.*, 1981]. Since the IMF and solar wind observations are based on measurements from an upstream solar wind monitor, they need to be time shifted to be representative for the upstream magnetopause. This can introduce errors unless the time shift is not properly done.

During our investigations, we noted that the distinct four-cell pattern seen for positive IMF B_z conditions (IMF Sector 0 in Figures 2 and 3) only emerged from the data if we did a careful selection and filtering of IMF data to ensure that only data obtained under stable northward IMF direction were selected. Any "contamination" of periods with southward IMF (which may occur, e.g, due to improper time shifting of solar wind data) tend to wipe out the four-cell pattern, since a southward IMF associated with a two-cell pattern is a much stronger driver. As in the H07 and F07 papers, we therefore made sure that only data from periods with stable IMF directions were selected. For this purpose, we applied the so-called bias vector estimation to IMF vector measurement with 1 min resolution over a time interval of 30 min that comprises 20 min before and 10 min after any actual EDI electric field measurment. The resulting normalized bias vector length, the bias value, can be considered as a measure for the stability of the IMF orientation over this interval. Like in the H07/F07 papers, a bias value of 0.96 was chosen in this study, filtering out all EDI data below this threshold.

Altogether, the convection patterns are very similar to those in H07 and patterns derived from ground-based data [see, e.g., *Ruohoniemi and Greenwald*, 2005; *Cousins and Shepherd*, 2010, and references therein]. In terms

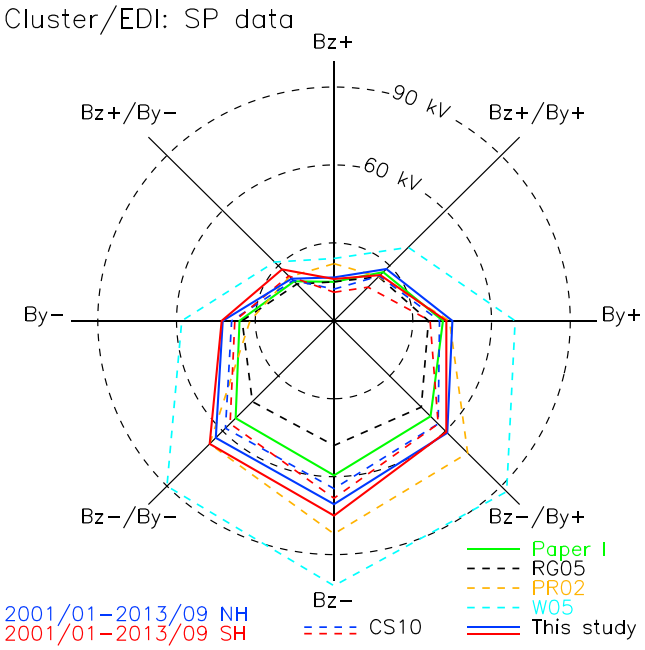

Figure 4. Comparison of cross polar cap potentials for various models for eight IMF orientations: Solid blue and red lines indicate results from the present study as shown in Figures 2 and 3 (blue = NH and red = SH). The green line indicates potential values from our previous EDI study reported in H07 (see text). The dashed black, orange, cyan, and blue/red lines are potentials reported by *Ruohoniemi and Greenwald* [2005], *Papitashvili and Rich* [2002], *Weimer* [2005], and *Cousins and Shepherd* [2010], respectively.

of shape, location, and size of the convection cells, there are no significant changes from the H07 results. There are minor subtleties though that become now more obvious with the more extended data set as will be shown below.

3.2. Cross Polar Cap Potential Values

For northward IMF (sector 0), potential difference values can be derived as the difference both between the two small dayside high-latitude lobe cells as well as between the main cells at lower latitudes; for the other patterns the CPCP is simply the difference between the minimum and maximum potential. In the NH, the CPCP varies from 70.6 kV for southward IMF to 16.7 kV for northward IMF. The corresponding SH CPCP values are fairly similar, with maximum and minimum values between 75.0 kV for southward IMF to 16.1 kV for northward IMF. The potential differences for the small dayside lobe cells are 14 kV and 8 kV in the NH and the SH, respectively.

Figure 4 shows a comparison between the present results and potentials derived from other sources. Values from the present study are shown as blue (NH) and red lines (SH), respectively. For comparison, we also show the average (from both hemispheres) from the H07 paper. Note that due to the bug explained in section 2.3, the potential values are not directly comparable to the results in H07 and F07. The potentials are similar to recent SuperDARN-based results reported by *Ruohoniemi and Greenwald* [2005], *Pettigrew et al.* [2010], and *Cousins and Shepherd* [2010], comparable in magnitude to the DMSP observations reported by *Papitashvili and Rich* [2002], but significantly smaller than predicted from the Weimer model [*Weimer*, 2005].

3.3. Error Source and Statistical Spread

Before proceeding to the discussion and implications of the above results, a few words about constraints, limitations underlying assumptions and accuracy of the results may be appropriate.

As any collection of experimental data, there are measurement errors. Fortunately, EDI provides very precise measurements. Errors introduced by mapping the EDI *E* field from the satellite position to the ionosphere, including the assumption of stationarity and equipotential magnetic field lines should also be small [*Woodfield et al.*, 2007].

Each of the convection maps in Figures 2 and 3 are based on a large number of individual measurements mapped and binned into small equal area bins in the ionosphere. Note that the statistical spread of the data entering each bin mostly represents genuine variability in the ionospheric flow and has a physical meaning [cf., e.g., F07, *Cousins and Shepherd*, 2012a, 2012b]. Large variability in the *E* field in a region can be the result of enhanced Poynting flux and heating.

More important are the constraints due to the way the data are collected. In particular, the data are not continuous in time but collected intermittently when Cluster has a magnetic foot point in the ionosphere. Since the Cluster orbit configuration means that different regions are covered at different seasons, no seasonal studies (or dipole tilt dependencies as in *Pettigrew et al.* [2010]) can be done.

3.4. Power Spectra of the Electric Field Potential

The procedure to construct the potential plots involves a step where the electrostatic potentials Φ are expanded in terms of a number of spherical harmonic functions [e.g., *Ruohoniemi and Baker*, 1998; *Ruohoniemi and Greenwald*, 2005].

$$\Phi(\theta,\phi) = \sum_{l=0}^{L} a_{l0} P_l^0(\cos\theta) + \sum_{l=1}^{L}\sum_{m=1}^{l} (a_{lm}\cos m\phi + b_{lm}\sin m\phi) P_l^m(\cos\theta) \quad (1)$$

where P_l^m are the associated Legendre polynomials with degree l and order m of the harmonic polynomials, a_{lm} and b_{lm} are real-valued coefficients. Every pair (l, m) of coefficients a_{lm} and b_{lm} in the series of spheric harmonics in equation (1) can be rewritten as amplitude and phase of this term:

$$|A_{lm}| = \sqrt{\left(a_{lm}^2 + b_{lm}^2\right)}, \quad \phi_{lm} = \arctan(a_{lm}, b_{lm}) \quad (2)$$

The basis functions of this spherical harmonic expansion describe different characteristic scales of the ionospheric convection pattern, and their associated coefficients can be regarded as the magnitude (electric potential values) of each basis function. This procedure is illustrated in a very informative way by *Grocott et al.* [2012].

We performed therefore a power spectra analysis of the electric potential distributions based on the fact that the coefficients of the associated Legendre polynomials can be represented by their amplitude $|A_{lm}|$ and argument or phase ϕ_{lm}, which gives the rotation in magnetic local time. The potential plots in Figures 2 and 3 are represented by associated Legendre polynomial expansions of degree $l = 8$ and order $m = 8$. The electrical potential is assumed to be zero at lower geomagnetic latitudes $\phi_m < 58°$, whereto EDI measurements do not map anyway, so that we made a transformation of the spherical cap $|\phi_m| \geq 58°$ to the whole sphere to be used for the spherical harmonic expansion, as described in H07.

Figure 5 shows the power distribution of the electric field potential coefficients versus the degree of the spherical harmonic series for all eight sectors in the NH (left) and SH (right). Due to the zero potential boundary conditions, the zero-degree coefficients are always zero. The spectra start with the dipole term $l = 1$, which represents the predominant term for all spectra, and decline sharply with increasing degree of the expansion.

The dipole term contains by far the most power of the EDI electrostatic distributions shown in Figures 2 and 3. The total power of the electric potential distributions for both the NH (blue line) and SH (red line) is presented in Figure 6 versus the IMF orientation or sector numbers. The power clearly maximizes for southward IMF (B_z-, sector 4), with slightly larger values for the SH in the case of this EDI data set. The minimum values are also clearly attained for purely northward IMF (B_z+, sector 0) in both hemispheres. Interestingly, the power distributions reveal a small shift relative to each other with respect to the IMF angle. The NH power spectra show a dominance for positive IMF B_y (sectors 1–3), while the SH electric field power prevails for negative IMF B_y orientations (sectors 5–7). This is most likely related to the magnetosphere-ionosphere interaction, namely, the contribution of the wind pattern of the neutral atmosphere, where the ionosphere is embedded. This atmospheric dynamo effect brings about this systematic shift (we come back to this in section 4.1).

The first few coefficients of the polynomials can further be systematically analyzed and reveal some characteristic order, as demonstrated by *Grocott et al.* [2012]. Here we confine to the first or dipole-order terms only.

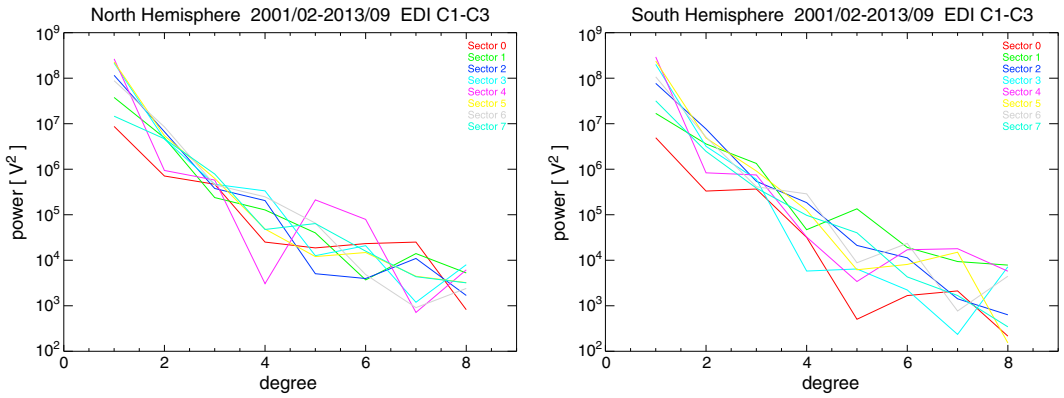

Figure 5. Power of the electric field potential coefficients (in [V^2]) versus degree of the spherical harmonics series for both (left) NH and (right) SH as shown in the potential plots of Figures 2 and 3, respectively, but now for the EDI Prime Parameter (PP) data set instead of SP. The various IMF sectors are indicated by different colors. The dipole term by far dominates the spectra of decreasing power with increasing degree numbers of the higher harmonics.

Figure 7 shows the amplitude and phase of the dipole term versus the IMF orientation. The sector numbers are given as labels of the respective data points. Maximum power values are again associated with southward IMF (B_z-, sector 4), and the minimum power values of the dipole term with northward IMF (B_z+, sector 0). The phase variation with the IMF orientation occurs in a very systematic way and with opposite orientations of the rotation in the NH and the SH in clockwise and anticlockwise direction, respectively, in this plane of the figure's projection. There are only a few minor deviations from this mirror symmetry. We observe a minor tendency for slightly larger phase shifts in the NH for the pairs of conjugate sectors, the most obvious for positive IMF B_z conditions and the sector pair 1 (NH) and 7 (SH). There seems to exist a breaking of symmetry for northward IMF conditions that could be due to specific magnetosphere-ionosphere-thermosphere coupling effects for the lobe cells. The significance of this effect has to be studied separately. For southward IMF (sector 4), an approximate phase shift of ~1 hr toward earlier magnetic local time in both hemispheres agrees with the fact that the sector 4 distributions in Figures 2 and 3 show both a slight clockwise turning that is obviously slightly larger in the NH for this data set. The dominant dipolar term of the electric field

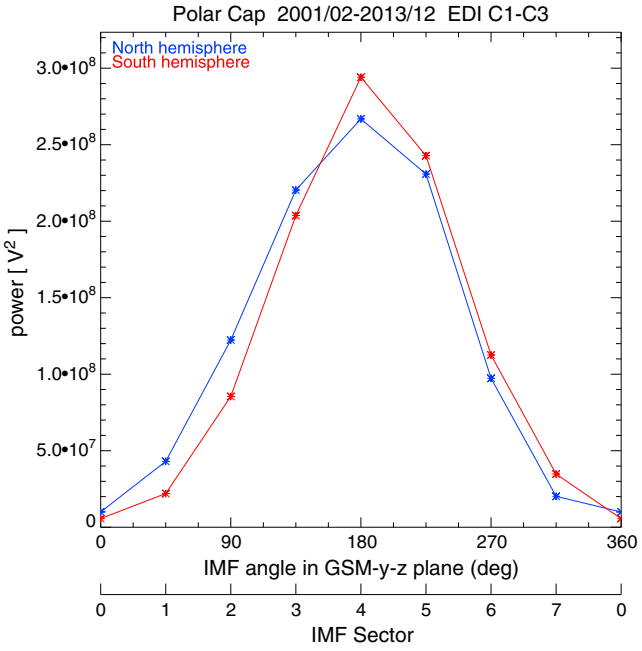

Figure 6. Total power of the electric field spherical harmonics potential series (in [V^2]) versus the IMF angle orientation (or IMF sector numbers) for both the NH (blue) and the SH (red). The same EDI data set and binning as in Figure 5 has been used here.

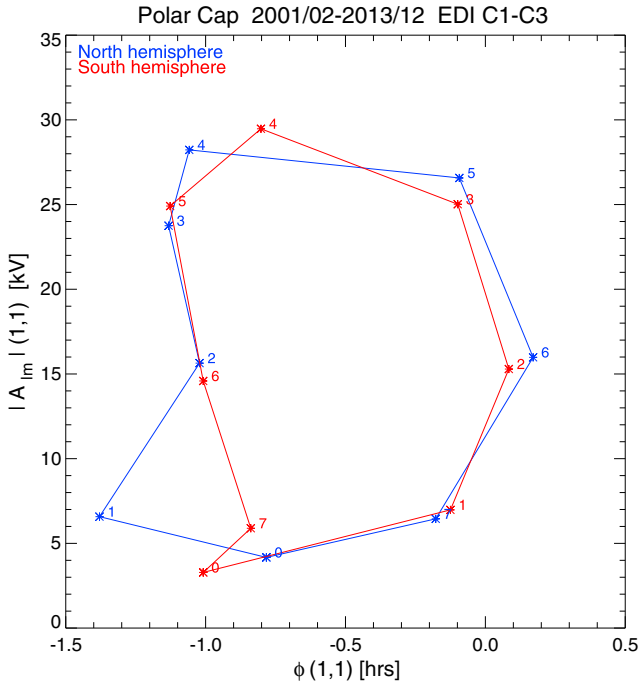

Figure 7. Power of the fundamental dipole terms $A_{1,1}$ versus their phase $\phi_{1,1}$ (in hours) of the spherical harmonics series [cf. *Grocott et al.*, 2012] for both NH (blue) and SH (red). The same EDI data set and binning as in Figures 5 and 6 has been used here. The numbers at the data points indicate the IMF sectors. Note the opposite orientation of the phase changes in the NH and the SH.

distribution determines this dominant large-scale two-cell convection pattern. The phases of the dipolar term associated with sector 5 and sector 3 for the NH and SH, respectively, are close to zero and constitute hence basically the straight cross polar flow almost aligned with the noon-midnight meridian.

3.5. Long-Term Effects

Figure 8, shows both the daily averages of the *Dst* index as well as the $F_{10.7}$ index over the whole time interval—i.e., more than one full solar cycle—of Cluster EDI observations. The latter is a measure of the solar activity or the "noise" generated by the Sun at a wavelength of 10.7 cm; higher values indicate higher solar activity. Daily values of the $F_{10.7}$ index are measured at local noon at the Penticton Radio Observatory in Canada. Historically, this index has been used as a proxy for the solar radiation output, and thus as an indicator of the solar cycle. The Cluster measurements started during years of high solar activity in 2001–2003, including some important "superstorm" periods as, e.g., the geomagnetically strong disturbance periods in fall 2003 with the famous Halloween storm on 29–30 October 2003. After a transition period with decreasing activity in 2004–2005, the Cluster EDI measurements also comprise several years of solar minimum conditions, including those years with extremely deep solar minimum conditions in 2007–2009.

The geomagnetic *Dst* index shows that there is on average also more electromagnetic power from the solar wind coupling during active periods with large peaks during storm periods. During the years of low solar activity also the frequency and intensity of these geomagnetic disturbance periods are considerably reduced. Larger *Dst* amplitudes means that there is on average more intense convection during the years of higher solar activity. This could also be shown with other geomagnetic parameters like, e.g., the polar cap indices and Akasofu's so-called "epsilon" parameter [*Perreault and Akasofu*, 1978].

We approached the question of possible solar activity dependences in the EDI data in two ways. First, we analyzed potential distributions for parts of the whole observation interval, and second, we calculated yearly statistical averages of the mean cross polar ion drift within the central polar cap at magnetic latitudes $\phi_m > 80°$.

Figure 9 shows the result of the latter approach for the comparison of yearly averages in both hemispheres. The plot shows the average convection velocity magnitude $|V|$ at high magnetic latitudes, and the average drifts in $-x$ and y direction in Solar Magnetospheric (SM) coordinates for both the NH (blue) and SH (red)

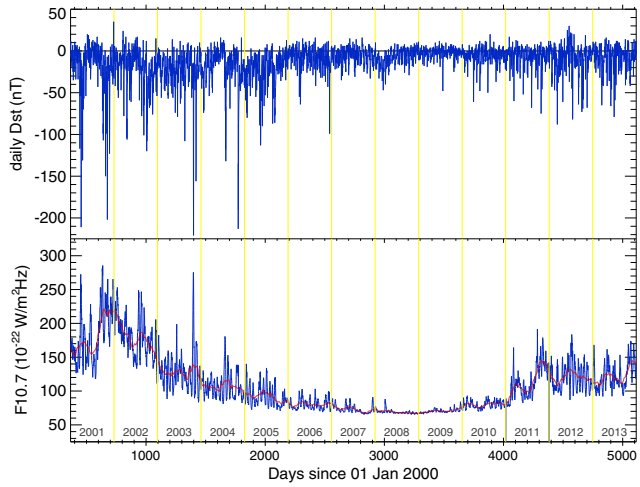

Figure 8. Solar cycle effects on ionospheric convection. (top) The daily *Dst* value (nT) shows geomagnetic activity, while (bottom) the $F_{10.7}$ solar radio flux index ($10^{-22} W/m^2 Hz$) is a proxy for solar activity. The red line shows the 81 day average (three Bartels' rotations) of the solar radio flux index.

during the years 2001–2008. The evolution of the Cluster orbits during subsequent years did not allow to continue these time series; the measurements did not map anymore to these high latitudes—first for the NH and later for the SH—due to the southward precession of the apsides.

Figure 9 (bottom) shows the relative data coverage for the yearly bins. The average convection drift magnitude maximizes in 2003 for both hemispheres and shows thereafter a decreasing trend until and including 2006. The SH values follow this tendency until the end of the observational interval (at these high magnetic latitudes) in 2008, while the NH shows a jump-like increase in 2007/2008.

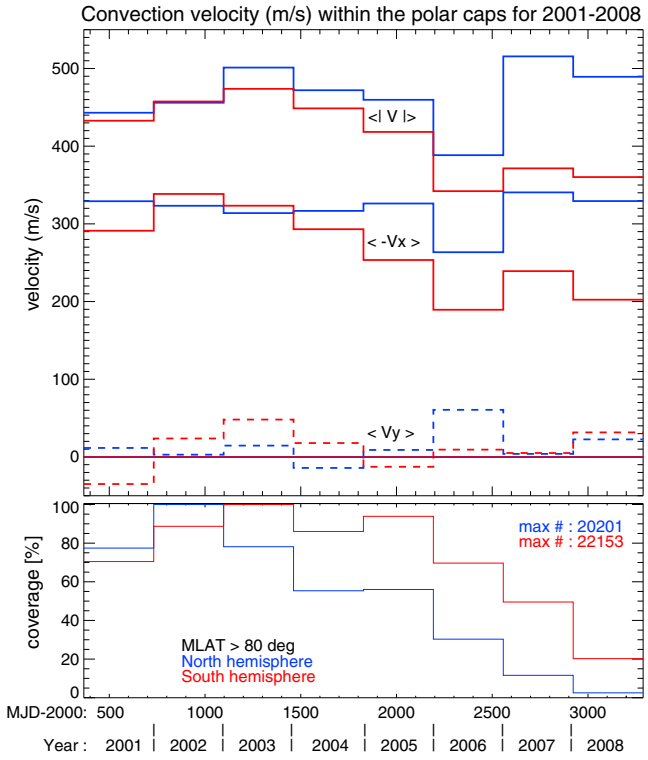

Figure 9. Yearly average ionospheric convection velocity at magnetic latitudes $|\phi_m| > 80°$ over the years 2001–2008, separately for the NH (blue) and the SH (red). The average values are shown for the velocity magnitude $|V|$ as well as for the $-V_x$ and V_y components. (bottom) The percentage of relative data coverage.

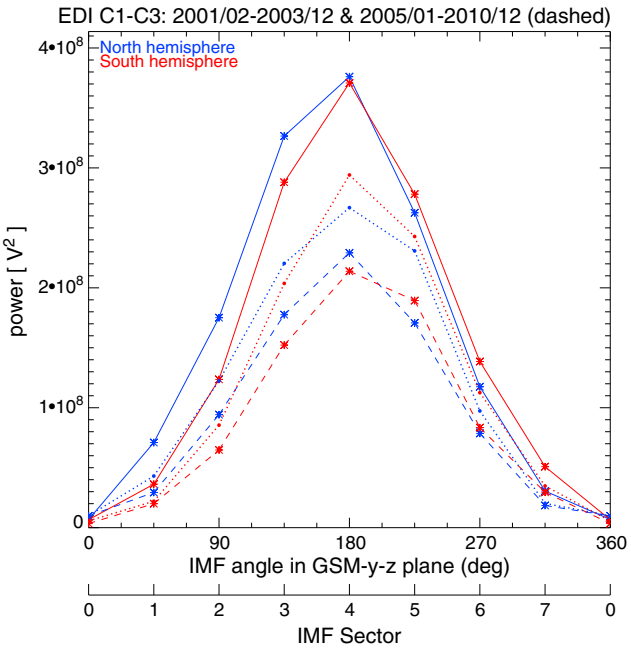

Figure 10. Solar cycle effects on ionospheric convection. Total power of the NH (blue) and SH (red) electric field spherical harmonics potential series (in [V^2]) versus the IMF angle orientation as in Figure 6 for years of high (2001–2003, solid lines) and low (2005–2010, dashed) solar activities. The curves of the full data set 2001–2013 are reproduced here from Figure 6 for comparison (dotted lines).

The jump could either be the result of the poor data coverage during these years in the NH or the consequence of an inappropriate orbit with the perigee over the NH during these years. The values of the negative (antisolar) component of the convection drift confirm the tendency of decreasing average drift velocities over the central polar cap with decreasing solar activity, while average values of the dawn-dusk component vary around zero.

Note that the average convection drift magnitudes in the NH have the tendency to be slightly larger than the SH averages. This is most likely related to the fact that the magnetic field strength at high latitudes is on average larger in the SH than in the NH. This is true in particular not only for the polar caps but also for large parts of the auroral and subauroral zones, i.e., on closed field lines (cf. Figure 12 below). *Förster and Cnossen* [2013] verified it by means of a numerical experiment that compares ion drift and neutral wind behavior at high latitudes by modeling both symmetric geomagnetic dipole and more realistic International Geomagnetic Reference Field (IGRF) conditions.

The generation of potential patterns as in Figures 2 and 3 requires a sufficiently good data coverage [cf., e.g., *Ruohoniemi and Baker*, 1998]. The low data availability in later years makes it difficult to obtain accurate potential values for these years. After some trials we made the following division of the whole observation interval into years of high to medium solar activity during 2001–2003 and years of low solar activity during 2005–2010.

The results of the CPCP estimations from the set of the eight IMF sectors for each of these portions and for the full time interval is listed in Table 1, while Figure 10 compares the corresponding total power distributions versus IMF sector. The solid lines stand for the high solar activity years 2001–2003, and the dashed curves for the low solar activity interval 2005–2010. While the general behavior including the opposite shift due to the IMF B_y dependence persists, the difference in power amplitude is evident. The difference of the power values between the high and low activity intervals attains a factor of about 75% for sector 4. The tendency for the high-activity power contents to be larger than those for low activity diminishes for purely northward IMF (sector 0) or even reverses in the NH ($6.8 \cdot 10^6$ V^2 versus $9.8 \cdot 10^6$ V^2 for the intervals 2001–2003 and 2005–2010, respectively) in contrast to the SH ($6.6 \cdot 10^6$ V^2 versus $3.4 \cdot 10^6$ V^2, respectively). This behavior for positive IMF B_z in the NH is in opposition to the general trend. It is also confirmed by the CPCP values of Table 1, first row.

The comparison of the CPCP values for high and low solar activity years in Table 1 reveals differences of about 30%–35% for the sectors with southward IMF orientation. The CPCP values for the whole interval lie

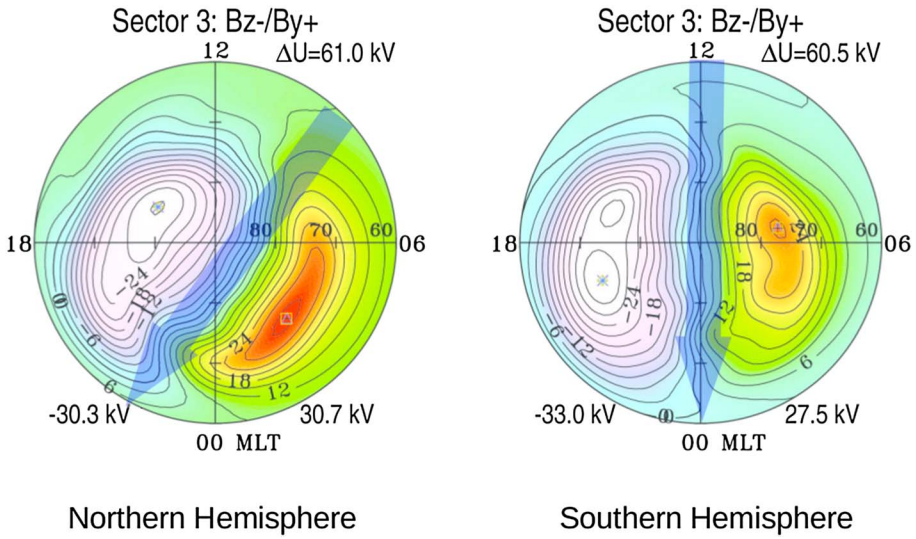

Figure 11. Illustration of IMF B_y influence on the north-south asymmetry. (left) The convection pattern for the NH and (right) the corresponding SH convection for identical IMF conditions. For this particular IMF configuration, the NH main flow channel (indicated by the overlaid blue arrow) is shifted and rotated and goes from around 09 MLT on the dayside to 22 MLT in the night side. For the SH, the main flow channel is essentially noon-midnight aligned.

somewhere in between. It is obvious that the CPCP values vary proportional to the solar activity level (with the exception of sector 0 in the NH as mentioned above). In all the cases, the SH values are slightly larger than the NH ones for negative IMF B_z (sector 4) conditions, and they are mostly slightly larger also for negative IMF B_y, while for positive B_y this can be reverse.

4. Discussion

We focus our discussion on two features of the new data set: the interhemispheric asymmetry and solar cycle signatures.

4.1. Interhemispheric Asymmetries

The dynamics in the ionosphere is largely controlled by two factors: external forcing from the solar wind-magnetosphere interaction on one hand and local conditions in the thermosphere and its embedded ionosphere on the other hand. Our results suggest that a north-south asymmetry due to the solar wind generator is most pronounced during strong driving (negative IMF B_z) and with IMF B_y penetration.

Figure 11, which is simply a reproduction of IMF sector 3 from Figures 2 and 3, highlights this asymmetry. For this IMF configuration, a negative IMF B_z combined with a positive IMF B_y, a clear north-south difference exists. Whereas the NH dial (Figure 11, left) shows a rotated and shifted convection pattern with the main flow channel between 09 magnetic local time (MLT) on the dayside and 22 MLT on the nightside, the SH (Figure 11, right) shows a nearly noon-midnight-aligned main flow channel. For IMF B_y negative (sector 5), the situation is essentially opposite, even with a more pronounced north-south difference of the CPCP values. These results confirm the previously known and well-documented IMF B_y asymmetry [*Ruohoniemi and Baker*, 1998; *Tanaka*, 2001; *Pettigrew et al.*, 2010]. Moreover, these pairs of potential patterns show very clearly the effect of ionospheric conductivity on breaking the symmetry between the hemispheres. The day-night conductivity gradient modifies the curvature of equipotential lines so that they concentrate on the dawnside as, e.g., in case of IMF B_z-/B_y+, shown in Figure 11 (left). This makes the dawn cell more crescent shaped and the dusk cell looking more round. The clockwise rotation of the nightside convection pattern by 1 – 2 h MLT that causes there a "kink" in the duskside cell can be understood by considering the effect due to Hall current closure of the Region 1 field-aligned current near the terminator line [*Atkinson and Hutchison*, 1978; *Tanaka*, 2001].

As suggested by *Förster et al.* [2008b], the curl-free noon-midnight-aligned plasma flow operates apparently in favor of an enhanced neutral wind acceleration across the polar cap. The straight plasma flow reinforces the diurnal neutral wind bulk flow from the early afternoon bulge across the polar region to the nightside caused by dayside (mainly EUV) heating. This "pressure valve" allows the largest cross polar thermospheric

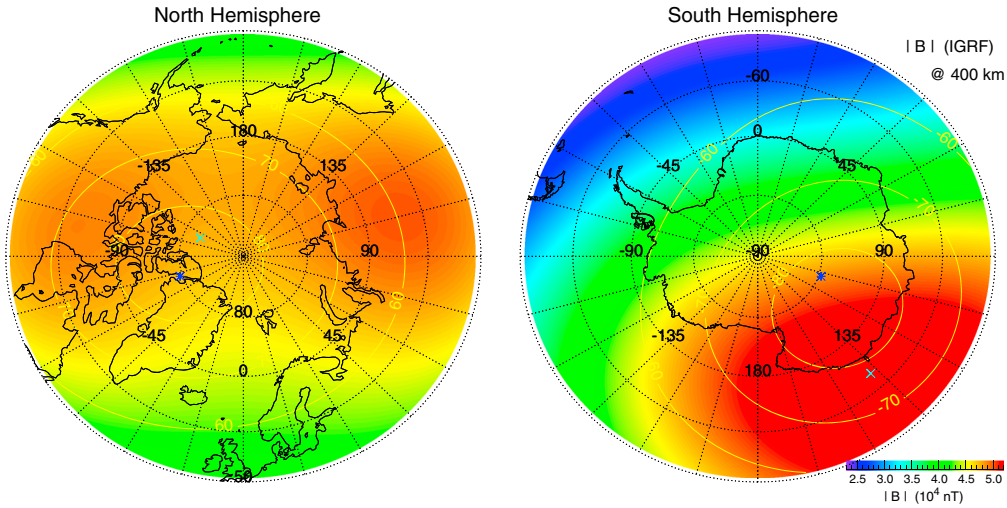

Figure 12. Color-coded maps of magnetic field strength at 400 km height for (left) the NH and (right) the SH in circular geographic coordinates around the poles with the color scale on the bottom right, which is valid for both panels. The outer borders are at ±50° geographic latitude; the longitudes are labeled near the ±70° parallel. The magnetic field in the NH is fairly homogeneous over large regions of the polar cap with magnetic field values ranging from around ∼ 40 μT to ∼ 50 μT. The magnetic field in the SH is characterized by larger anomalies and field values ranging from ∼ 24 μT to ∼ 54 μT. The dipole axis orientation (geomagnetic poles) are indicated with dark blue asterisks and the magnetic poles (or dip pole positions) with light blue crosses. The yellow isolines show geomagnetic parallels of altitude-adjusted corrected geomagnetic coordinates (AACGM).

wind amplitudes for IMF angle ranges corresponding to sector 5 in the NH and sector 3 in the SH as could be revealed recently from CHAMP accelerometer measurements [*Förster et al.*, 2008b, 2011].

On the other hand, the thermospheric wind moves the conducting ionized layers across the geomagnetic field lines, resulting in a neutral wind dynamo effect that contributes to the overall electrodynamics of the coupled system [*Blanc and Richmond*, 1980]. The inertia of the upper atmosphere supports to maintain the ionospheric convection independently of the magnetospheric driver processes, which is known for long time as a "fly-wheel effect" of the upper atmosphere [*Banks*, 1972; *Coroniti and Kennel*, 1973].

The systematic NH-SH differences for the high-latitude upper atmosphere parameters appear to be even larger with respect to the neutral wind dynamics. Based on CHAMP accelerometer data, *Förster et al.*, 2008b [2008b, 2011] showed also that the average high-latitude neutral wind vorticity at ∼ 400 km altitude in the NH can exceed that in the SH by up to 30% during years of moderate to high solar activity.

Simulations with the Coupled Magnetosphere-Ionosphere-Thermosphere model have recently demonstrated that these differences can be explained at least to some extent by asymmetries in the Earth's magnetic field, both in magnetic flux density and in the offset between the geographic and invariant magnetic poles in the two hemispheres [*Förster and Cnossen*, 2013].

Figure 12 shows color-coded maps of the geomagnetic field as given by the International Geomagnetic Reference Field (IGRF). In the NH polar cap region, the magnetic field is fairly homogeneous over large regions, with magnetic field magnitudes ranging from around ∼ 40 μT to ∼ 50 μT. The angle between the rotation axis and the magnetic axis is less than 10° for the epoch relevant to our study. In the SH, there is a much larger spatial variation in the magnetic field magnitude, and the offset between the rotation axis and the invariant geomagnetic axis is about twice as large compared to the NH (∼ 16° versus ∼ 8°, respectively). For a given potential difference imposed by the solar wind magnetosphere interaction, this implies that the local ionospheric electric field, given by $\vec{E} = -\nabla\Phi$ (Φ being the electrostatic potential, equation (1)), will be different in the two hemispheres.

Small differences of the CPCP values between the NH and the SH have been found by other researchers with different observational means. *Papitashvili and Rich* [2002] found from DMSP observations that the CPCPs are slightly asymmetric even during equinox with a north/south ratio of 0.9. They suggest that the Region 1 field-aligned currents may not be supplied equally to both polar regions due to the interhemispheric

geometrically imbedded asymmetry in the overall configuration of the main geomagnetic field and the magnetospheric field sources but admit also that variations in the ionospheric conductivity may also contribute to this effect.

Pettigrew et al. [2010] found that the convection patterns are generally symmetric between hemispheres, except during IMF B_z- conditions for all tilts, when the CPCP is systematically larger (by 6.5% according to their estimate) in the SH than in the NH. Further, they state that the CPCP values are larger during B_y- (B_y+) in the north (south) under neutral tilt, when the CPCP is larger in the north. The dawn and dusk potentials vary more with tilt than does the CPCP, and they are more interhemispherically asymmetric.

Our results support the view that on average the CPCP values in the SH are slightly (∼5%–7%) larger than those in the NH. This high-latitude electric potential disparity is on average somehow more distinct for negative IMF B_y conditions compared with positive IMF B_y, at least during moderate to high solar activity (cf. Figure 4 and Table 1). The observation of slightly larger drift velocities in the NH compared with the SH (Figure 9) contradicts this statement only apparently. The different magnetic field strength obviously overcompensates due to the inverse dependence of $V \sim E/B$ the larger potential difference (electric field strength) values in the SH. This is a simplified view that assumes equal distances between the potential foci and homogeneous potential distributions across the polar cap, which is not necessarily fulfilled. Global physical-numerical model studies could help to clarify the situation.

4.2. Solar Cycle Signatures

The EDI Cluster observations cover now more than a solar cycle, so that it was suggesting itself to investigate this question more closely. We approached it with all available data sets: the standard SP, the PP, and a further particular "Special Good" (SG) selection that considered only those EDI measurements with the highest-quality stamp.

First, we considered yearly averages of the convection magnitude and its horizontal components within the central polar cap at magnetic latitudes $|\phi_m| > 80°$ as it is shown in Figure 9. The idea behind this method is that the average plasma drift can serve in "zero-order" approximation as a proxy of the CPCP (see F07, Figures 7–9). Such statistics can be executed also with smaller amounts of data, which possibly not just yet allow the reconstruction of potential patterns. As has been shown by this study, this approach is constraint by the hemispheric differences of high-latitude magnetic field strength and configuration.

Figure 9 shows the results for SP EDI data, but the general outcome for all other EDI data sets is the same (not shown here). The maximum ionospheric drift magnitudes over the central polar cap were observed in 2003 during the year of high solar activity and frequent and sometimes very strong geomagnetic disturbances like the superstorms in October–November 2003 (see Figure 8).

During 2001–2002 we observe slightly smaller drift velocity averages, although the solar activity, as reflected by the $F_{10.7}$ index, was even larger during these years. This suggests that the solar wind and IMF driver of geomagnetic disturbances are probably more important for an enhanced level of average ionospheric drift magnitudes than the solar EUV activity (or the degree of ionization in the upper atmosphere).

After 2003 we observe a steady trend of declining average drift magnitude in both hemispheres, which persists in the SH until the end of the observation period. Afterward, the evolution of the Cluster orbits preclude this kind of statistics as the foot points of observations in the NH shifted toward lower magnetic latitudes. The jump-like increase in 2007/2008 in the NH are most likely due to the location of Cluster which was, on average, closer to the nearby auroral region during these years. The open-closed magnetic field line boundary (OCB) marks the transitions between open and closed geomagnetic field lines that is equivalent to the reconnection separatrix for most IMF conditions, alternatively termed the polar cap boundary [*Chisham et al.*, 2008]. Long-term satellite observations have readily shown reconnection to involve transient, rapidly varying (with timescales of minutes) processes of sudden enhanced ion fluxes such as flux transfer events (FTEs), localized near the dayside magnetopause [*Russell and Elphic*, 1978]. Using ground-based radar techniques and auroral imager data from satellites, there are attempts to determine the OCB position in the ionosphere for the estimation of reconnections rates near to this boundary both on the dayside and nightside auroral ovals [*Pinnock et al.*, 1999, 2003; *Østgaard et al.*, 2005]. For this study, we excluded (like in H07 and F07) all data points within 2 R_E distance from the (model) magnetopause and the plasma sheet to minimize the effect of such enhanced flux events.

A rough estimate of drift magnitudes inside the polar cap between years of high to medium and low solar activities with $|V_{high}|/|V_{low}| \approx (450\text{m/s})/(350\text{m/s})$ and $|Vx_{high}|/|Vx_{low}| \approx (-320\text{m/s})/(-240\text{m/s})$ results in a difference of about 30% (considering only the SH results in Figure 9). This should approximately correspond to equally large differences in the CPCP values.

The alternative way to study the solar activity dependence by means of reconstructing complete high-latitude convection patterns was best done with the PP data set, while the other data sets are affected by potential distribution artifacts of the spherical harmonic series due to gaps in the data coverage. The results shown in Table 1 for the PP EDI data reveals the same tendency as the statistical method above. For the years of higher solar and geomagnetic activities 2001–2003 we observe up to 30%–35% larger CPCP values than during the years of solar minimum. For better quantitative analyses one should apply different methods like, e.g., the Empirical Orthogonal Function (EOF) analysis, which is beyond the scope of this paper.

5. Summary

More than 10,000 h Cluster EDI observations for each hemisphere over the last 13 years covering a full solar cycle resulted in rich statistical material and form a solid base for the following main findings.

As many previous studies revealed already, the IMF strength and orientation is a major ruling factor for the convection pattern shape and rotation with respect to the magnetic noon-midnight meridian. Generally, we find a two-cell convection for all IMF orientations with the exception of purely northward IMF, where additionally appears a minor convection cell pair at higher latitudes on the dayside with the opposite polarity.

The dominant two-cell pattern corresponds to the fact that the dipolar term of the associated Legendre polynomial series, which represents the potential field of the high-latitude ionospheric convection, is by far the largest term for all IMF orientations. It contains the most power of the potential electric field.

The phase of this dipolar term shows that the IMF B_y component determines also the rotation of the main two-cell convection pattern with respect to the noon-midnight meridian. The phase change has an opposite orientation in the opposite hemispheres.

In addition to this generally opposite IMF B_y behavior, there is a relative shift of the power distribution to each other between the hemispheres that depends on the IMF B_y sign. This shift is obviously due to the feedback action of the atmospheric generator on the large-scale magnetospheric convection electric field. There is a tendency for larger power content for positive IMF B_y in the NH and larger power content for negative IMF B_y in the SH compared with the respective opposite hemisphere.

This relation can also reflect in CPCP values but not as a one-to-one relation. However, for negative IMF B_y the CPCP values in the SH are to a greater extent larger than in the NH than for positive IMF B_y conditions. On average over all conditions, the CPCP values in the SH are larger than in the NH by about 5%–7%.

Further, we observe qualitatively an obvious solar acitivity dependence of the electric field potential power on the solar (and geomagnetic) activity level. The average difference during the operational period of Cluster between high solar activity conditions in 2001–2003 compared with low solar activity in 2005–2010 amounts to ~75% (in units of $[V^2]$) or ~30%–35% for the CPCP values (in $[V]$). These estimates correspond approximately to each other.

We suggest that the observed hemispheric differences in the electric field potential pattern are largely due to significant differences in the strength and configuration of the geomagnetic field between the NH and SH. These differences will also affect the local ionospheric conditions like conductivity distributions that result in their own feedback to the electric field potential distribution of the coupled magnetosphere-ionosphere-thermosphere system.

Acknowledgments
Work at GFZ German Research Centre for Geosciences Potsdam (M. F.) was supported by Deutsche Forschungsgemeinschaft (DFG). S.H. acknowledges support from the Norwegian Research Council, grant 223252/F50. The authors thank the International Space Science Institute, Bern, Switzerland for providing computer resources and infrastructure for data exchange. Computer code used for the calculations in this paper has been made available as part of the QSAS science analysis system, provided by the United Kingdom Cluster Science Centre (Imperial College London and Queen Mary, University of London). A numerical IDL code of the IMF-dependent high-latitude EDI convection patterns of both hemispheres can be obtained on request from the authors and will be available via the web address of section 2.3 at GFZ (http://www.gfz-potsdam.de/en/section/earths-magnetic-field/).

The Editor thanks two anonymous reviewers for their assistance in evaluating this paper.

References

A, E., A. J. Ridley, D. Zhang, and Z. Xiao (2012), Analyzing the hemispheric asymmetry in the thermospheric density response to geomagnetic storms, *J. Geophys. Res.*, *117*, A08317, doi:10.1029/2011JA017259.

Atkinson, G., and D. Hutchison (1978), Effect of the day night ionospheric conductivity gradient on polar cap convective flow, *J. Geophys. Res.*, *83*, 725–729.

Baker, K. B., and S. Wing (1989), A new magnetic coordinate system for conjugate studies at high latitudes, *J. Geophys. Res.*, *94*, 9139–9143.

Banks, P. M. (1972), Magnetospheric processes and the behavior of the neutral atmosphere, *Space Res.*, *12*, 1051–1067.

Barlier, F., C. Jaeck, P. Bauer, G. Thullier, and G. Kockarts (1974), North-south asymmetries in the thermosphere during the last maximum of the solar cycle, *J. Geophys. Res.*, *79*, 5273–5285.

Blanc, M., and A. D. Richmond (1980), The ionospheric disturbance dynamo, *J. Geophys. Res.*, *85*, 1669–1686.
Chisham, G., et al. (2008), Remote sensing of the spatial and temporal structure of magnetopause and magnetotail reconnection from the ionosphere, *Rev. Geophys.*, *46*, RG1004, doi:10.1029/2007RG000223.
Coroniti, F. V., and C. F. Kennel (1973), Can the ionosphere regulate magnetospheric convection?, *J. Geophys. Res.*, *78*, 2837–2851.
Cousins, E. D. P., and S. G. Shepherd (2010), A dynamical model of high-latitude convection derived from SuperDARN plasma drift measurements, *J. Geophys. Res.*, *115*, A12329, doi:10.1029/2010JA016017.
Cousins, E. D. P., and S. G. Shepherd (2012a), Statistical characteristics of small-scale spatial and temporal electric field variability in the high-latitude ionosphere, *J. Geophys. Res.*, *117*, A03317, doi:10.1029/2011JA017383.
Cousins, E. D. P., and S. G. Shepherd (2012b), Statistical maps of small-scale electric field variability in the high-latitude ionosphere, *J. Geophys. Res.*, *117*, A12304, doi:10.1029/2012JA017929.
Dungey, J. W. (1961), Interplanetary magnetic field and the auroral zones, *Phys. Rev. Lett.*, *6*, 47–48.
Eriksson, A. I., et al. (2006), Electric field measurements on Cluster: Comparing the double-probe and electron drift techniques, *Ann. Geophys.*, *24*, 275–289.
Escoubet, C. P., A. Pedersen, R. Schmidt, and P. A. Lindqvist (1997), Density in the magnetosphere inferred from ISEE 1 spacecraft potential, *J. Geophys. Res.*, *102*, 17,595–17,609.
Förster, M., and I. Cnossen (2013), Upper atmosphere differences between northern and southern high latitudes: The role of magnetic field asymmetry, *J. Geophys. Res. Space Physics*, *118*, 5951–5966, doi:10.1002/jgra.50554.
Förster, M., G. Paschmann, S. E. Haaland, J. M. Quinn, R. B. Torbert, C. E. McIlwain, H. Vaith, P. A. Puhl-Quinn, and C. A. Kletzing (2007), High-latitude plasma convection from Cluster EDI: Variances and solar wind correlations, *Ann. Geophys.*, *25*, 1691–1707.
Förster, M., S. E. Haaland, G. Paschmann, J. M. Quinn, R. B. Torbert, H. Vaith, and C. A. Kletzing (2008a), High-latitude plasma convection during northward IMF as derived from in-situ magnetospheric Cluster EDI measurements, *Ann. Geophys.*, *26*, 2685–2700.
Förster, M., S. Rentz, W. Köhler, H. Liu, and S. E. Haaland (2008b), IMF dependence of high-latitude thermospheric wind pattern derived from CHAMP cross-track measurements, *Ann. Geophys.*, *26*, 1581–1595.
Förster, M., S. E. Haaland, and E. Doornbos (2011), Thermospheric vorticity at high geomagnetic latitudes from CHAMP data and its IMF dependence, *Ann. Geophys.*, *29*, 181–186.
Förster, M., Y. I. Feldstein, L. I. Gromova, L. A. Dremukhina, A. E. Levitin, and S. E. Haaland (2013), Some aspects of modelling the high-latitude ionospheric convection from Cluster/EDI data, *Geomag. Aeron.*, *53*, 91–101.
Grocott, A., T. K. Yeoman, S. E. Milan, and S. W. H. Cowley (2005), Interhemispheric observations of the ionospheric signature of tail reconnection during IMF-northward non-substorm intervals, *Ann. Geophys.*, *23*, 1763–1770.
Grocott, A., S. E. Milan, S. M. Imber, M. Lester, and T. K. Yeoman (2012), A quantitative deconstruction of the morphology of high-latitude ionospheric convection, *J. Geophys. Res.*, *117*, A05317, doi:10.1029/2012JA017580.
Gustafsson, G. (1984), Corrected geomagnetic coordinates for epoch 1980, in *Magnetospheric Currents, Geophys. Monogr. Ser.*, vol. 28, edited by T. A. Potemra, pp. 276–282, AGU, Washington, D. C.
Haaland, S. E., G. Paschmann, M. Förster, J. M. Quinn, R. B. Torbert, C. E. McIlwain, H. Vaith, P. A. Puhl-Quinn, and C. A. Kletzing (2007), High-latitude plasma convection from Cluster EDI measurements: Method and IMF-dependence, *Ann. Geophys.*, *25*, 239–253.
Laundal, K. M., and J. W. Gjerloev (2014), What is the appropriate coordinate system for magnetometer data when analyzing ionospheric currents?, *J. Geophys. Res. Space Physics*, *119*, 8637–8647, doi:10.1002/2014JA020484.
Liou, K. (2010), Polar Ultraviolet Imager observation of auroral breakup, *J. Geophys. Res.*, *115*, A12219, doi:10.1029/2010JA015578.
Liou, K., P. T. Newell, C.-I. Meng, M. Brittnacher, and G. Parks (1998), Characteristics of the solar wind controlled auroral emissions, *J. Geophys. Res.*, *103*, 17,543–17,558.
Nishitani, N., V. O. Papitashvili, T. Ogawa, N. Sato, H. Yamagishi, A. S. Yukimatu, and F. J. Rich (2003), Interhemispheric asymmetry of the high-latitude ionospheric convection on 11–12 May 1999, *J. Geophys. Res.*, *108*(A5), 1184, doi:10.1029/2002JA009680.
Østgaard, N., N. A. Tsyganenko, S. B. Mende, H. U. Frey, T. J. Immel, M. Fillingim, L. A. Frank, and J. B. Sigwarth (2005), Observations and model predictions of substorm auroral asymmetries in the conjugate hemispheres, *Geophys. Res. Lett.*, *32*, L05111, doi:10.1029/2004GL022166.
Papitashvili, V. O., and F. J. Rich (2002), High-latitude ionospheric convection models derived from Defense Meteorological Satellite Program ion drift observations and parameterized by the interplanetary magnetic field strength and direction, *J. Geophys. Res.*, *107*(A8), 1198, doi:10.1029/2001JA000264.
Paschmann, G., et al. (2001), The electron drift instrument on cluster: Overview of first results, *Ann. Geophys.*, *19*, 1273–1288.
Perreault, P., and S.-I. Akasofu (1978), A study of geomagnetic storms, *Geophys. J. R. Astron. Soc.*, *54*, 547–573.
Pettigrew, E. D., S. G. Shepherd, and J. M. Ruohoniemi (2010), Climatological patterns of high-latitude convection in the northern and southern hemispheres: Dipole tilt dependences and interhemispheric comparisons, *J. Geophys. Res.*, *115*, A07305, doi:10.1029/2009JA014956.
Pinnock, M., A. S. Rodger, K. B. Baker, G. Lu, and M. Hairston (1999), Conjugate observations of the day-side reconnection electric field: A GEM boundary layer campaign, *Ann. Geophys.*, *17*, 443–454.
Pinnock, M., G. Chisham, I. J. Coleman, M. P. Freeman, M. Hairston, and J.-P. Villain (2003), The location and rate of dayside reconnection during an interval of southward interplanetary magnetic field, *Ann. Geophys.*, *21*, 1467–1482.
Quinn, J. M., et al. (2001), Cluster EDI convection measurements across the high-latitude plasma sheet boundary at midnight, *Ann. Geophys.*, *19*, 1669–1681.
Reiff, P. H., R. W. Spiro, and T. W. Hill (1981), Dependence of polar cap potential drop on interplanetary parameters, *J. Geophys. Res.*, *86*, 7639–7648.
Reistad, J. P., N. Østgaard, K. M. Laundal, S. Haaland, P. Tenfjord, K. Snekvik, K. Oksavik, and S. Milan (2014), Intensity asymmetries in the dusk sector of the poleward auroral oval due to IMF Bx, *J. Geophys. Res. Space Physics*, *119*, 9497–9507, doi:10.1002/2014JA020216.
Ruohoniemi, J. M., and K. B. Baker (1998), Large-scale imaging of high-latitude convection with Super Dual Auroral Radar Network HF radar observations, *J. Geophys. Res.*, *103*, 20,797–20,811.
Ruohoniemi, J. M., and R. A. Greenwald (2005), Dependencies of high-latitude plasma convection: Consideration of interplanetary magnetic field, seasonal, and universal time factors in statistical patterns, *J. Geophys. Res.*, *110*, A09204, doi:10.1029/2004JA010815.
Russell, C. T., and R. C. Elphic (1978), Initial ISEE magnetometer results: Magnetopause observations, *Space Sci. Rev.*, *22*, 681–715.
Sonnerup, B. U., G. Paschmann, I. Papamastorakis, N. Sckopke, G. Haerendel, S. J. Bame, J. R. Asbridge, J. T. Gosling, and C. T. Russell (1981), Evidence for magnetic field reconnection at the Earth's magnetopause, *J. Geophys. Res.*, *86*(A12), 10,049–10,067, doi:10.1029/JA086iA12p10049.
Tanaka, T. (2001), Interplanetary magnetic field by and auroral conductance effects on high-latitude ionospheric convection patterns, *J. Geophys. Res.*, *106*, 24,505–24,516.

Tsyganenko, N. A. (2002a), A model of the near magnetosphere with a dawn-dusk asymmetry 1. Mathematical structure, *J. Geophys. Res.*, *107*(A8), 1179, doi:10.1029/2001JA000219.

Tsyganenko, N. A. (2002b), A model of the near magnetosphere with a dawn-dusk asymmetry 2. Parameterization and fitting to observations, *J. Geophys. Res.*, *107*(A8), 1176, doi:10.1029/2001JA000220.

Walsh, A. P., et al. (2014), Dawn-dusk asymmetries in the coupled solar wind-magnetosphere-ionosphere system: A review, *Ann. Geophys.*, *32*, 705–737.

Watanabe, M., G. J. Sofko, K. Kabin, R. Rankin, A. J. Ridley, C. R. Clauer, and T. I. Gombosi (2007), Origin of the interhemispheric potential mismatch of merging cells for interplanetary magnetic field B_Y-dominated periods, *J. Geophys. Res.*, *112*, A10205, doi:10.1029/2006JA012179.

Weimer, D. R. (2005), Improved ionospheric electrodynamic models and application to calculating Joule heating rates, *J. Geophys. Res.*, *110*, A05306, doi:10.1029/2004JA010884.

Wild, J. A., et al. (2003), Coordinated interhemispheric SuperDARN radar observations of the ionospheric response to flux transfer events observed by the Cluster spacecraft at the high-latitude magnetopause, *Ann. Geophys.*, *21*, 1807–1826.

Wilder, F. D., C. R. Clauer, J. B. H. Baker, E. D. P. Cousins, and M. R. Hairston (2011), The nonlinear response of the polar cap potential under southward IMF: A statistical view, *J. Geophys. Res.*, *116*, A12229, doi:10.1029/2011JA016924.

Woodfield, E. E., M. W. Dunlop, R. Holme, J. A. Davies, and M. A. Hapgood (2007), A comparison of Cluster magnetic data with the Tsyganenko 2001 model, *J. Geophys. Res.*, *112*, A06248, doi:10.1029/2006JA012217.

Yeoman, T. K., R. V. Lewis, H. Khan, S. W. H. Cowley, and J. M. Ruohoniemi (2000), Interhemispheric observations of nightside ionospheric electric fields in response to IMF Bz and By changes and substorm pseudobreakup, *Ann. Geophys.*, *18*, 897–907.